

Production characteristics of light (anti-)nuclei from (anti-)nucleon coalescence in heavy ion collisions at energies employed at the RHIC beam energy scan

Xiang-Yu Zhao,¹ Yan-Ting Feng,¹ Feng-Lan Shao^{1,*}, Rui-Qin Wang^{1,†} and Jun Song^{2,‡}

¹*School of Physics and Physical Engineering, Qufu Normal University, Shandong 273165, China*

²*School of Physical Science and Intelligent Engineering, Jining University, Shandong 273155, China*



(Received 25 January 2022; accepted 2 May 2022; published 18 May 2022)

With the kinetic freeze-out nucleons and antinucleons obtained from the quark combination model, we study the production of light nuclei and antinuclei in the (anti-)nucleon coalescence mechanism in relativistic heavy ion collisions. We derive analytic formulas of the momentum distributions of different light nuclei and apply them to compute transverse momentum (p_T) spectra of (anti-)deuterons (d, \bar{d}) and (anti-)tritons (t, \bar{t}) in Au-Au collisions at $\sqrt{s_{NN}} = 7.7, 11.5, 19.6, 27, 39, 54.4$ GeV. We find that the experimental data available for these p_T spectra can be well reproduced. We further study the yields and yield ratios of different light (anti-)nuclei and naturally explain their interesting behaviors as a function of the collision energy. We especially point out that the multiparticle yield ratio tp/d^2 should be carefully corrected from hyperon weak decays for protons to probe the production characteristics of light nuclei. All of our results show that the coalescence mechanism for (anti-)nucleons plays a dominant role for the production of light nuclei and antinuclei at the BNL Relativistic Heavy Ion Collider beam energy scan energies.

DOI: [10.1103/PhysRevC.105.054908](https://doi.org/10.1103/PhysRevC.105.054908)

I. INTRODUCTION

Light nuclei and antinuclei such as (anti-)deuterons and (anti-)tritons are considered to be a unique kind of probe in ultrarelativistic heavy ion collisions. On one hand, they can effectively explore the information of the bulk system, especially the system freeze-out properties such as the geometrical freeze-out volume [1,2] and freeze-out particle correlations [3], etc., since they are mostly produced at the late stage of the system evolution. On the other hand, the production of such composite particles itself is very much well worth studying and it is closely related with many fundamental issues in high energy physics and in the astronomy field, e.g., the hadronization mechanism [4], cosmic-ray production, and propagation in the galaxy [5], etc.

In recent years the theoretical study of the production of light (anti-)nuclei has reabsorbed a lot of attention in heavy ion collisions [6–10]. Two production mechanisms have proved to be particularly successful in describing the light nuclei formation. One is the thermal production [11–16], which

assumes that (anti-)nuclei are produced from a thermally and chemically equilibrated source like abundantly produced mesons and baryons. The other is the coalescence mechanism [1,3,17–31], in which light (anti-)nuclei are assumed to be produced by the coalescence of the jacent (anti-)nucleons in the phase space. Such a production mechanism possesses its unique characteristics. Many specific models and/or event generators such as hybrid dynamical model (iEBE-MUSIC) [32], the ultrarelativistic-quantum-molecular-dynamics model (UrQMD) [33], jet AA microscopic transportation model (JAM) [34], the parton and hadron cascade model (PACIAE) [35], etc., have been developed to include light nuclei formation via the nucleon coalescence and provided nice explanations for series of observables. Besides these two mechanisms, a transport scenario is also proposed for light nuclei production, which assumes the existence of light nuclei in strongly interacting hadronic matter and aims to study how light nuclei evolve during the hadronic system evolution [36–39].

Experiments at the BNL Relativistic Heavy Ion Collider (RHIC) and the CERN Large Hadron Collider (LHC) have accumulated a wealth of data on light nuclei production. These data exhibit some fascinating features [40–45], especially their nontrivial energy-dependent behaviors at RHIC energies. Such behaviors are considered to be possible signals for the critical end point (CEP) of the first order phase transition from hadronic phase to quark-gluon phase in some works such as in Refs. [34,46]. As we know, the whole process of the relativistic heavy-ion collision is a very complicated process, involving many components, e.g., hard parton

*shaofl@mail.sdu.edu.cn

†wangrq@qfnu.edu.cn

‡songjun2011@jnxu.edu.cn

Published by the American Physical Society under the terms of the [Creative Commons Attribution 4.0 International](https://creativecommons.org/licenses/by/4.0/) license. Further distribution of this work must maintain attribution to the author(s) and the published article's title, journal citation, and DOI. Funded by SCOAP³.

scatterings, collective expansion evolution, hadronization, hadronic rescatterings, resonance decays, and so on. These components are very different in different centrality collisions at different energies and they finally lead to very different hadronic systems at the kinetic freeze-out. Is the nucleon coalescence a universal mechanism for light nuclei production in these different hadronic systems? Are the above nonmonotonic energy-dependent behaviors of light nuclei, usually taken as possible signals for the CEP, caused by the differences of the hadronic systems at different collision energies or by the production mechanism itself?

In this article, we apply the coalescence mechanism to hadronic systems created in Au-Au collisions at RHIC energies to study the production of light (anti-)nuclei in the low- and intermediate- p_T regions. One main goal of this article is to bring to light the characteristics originating mainly from the nucleon coalescence and to discriminate influences of different factors in heavy ion collisions on light nuclei production. For this purpose, we begin with the kinetic freeze-out nucleons and antinucleons obtained from the quark combination model developed by the Shandong group [47,48], and then we let these nucleons coalesce into different (anti-)nuclei to study their production characteristics. We find that weak decay contaminations for protons from Λ and Ξ hyperons are different in different centralities at different collision energies, and this should be carefully considered when using some light nuclei yield ratios related with protons measured by the STAR Collaboration, such as the multiparticle yield ratio $t p/d^2$, to probe the production characteristics of light nuclei and extract the CEP signal.

The rest of the article is organized as follows. In Sec. II, we give an introduction to the derivation of the momentum distributions of light nuclei in the framework of the nucleon coalescence. In Sec. III, we systematically study the p_T spectra and midrapidity yield densities of d , \bar{d} , t , \bar{t} in different centralities in Au-Au collisions at $\sqrt{s_{NN}} = 7.7, 11.5, 19.6, 27, 39, 54.4$ GeV. We present in particular various yield ratios of light nuclei such as d/p , \bar{d}/\bar{p} , t/p , \bar{t}/\bar{p} , d/p^2 , \bar{d}/\bar{p}^2 , $t p/d^2$, etc., and discuss their properties as functions of the collision energy and the collision centrality. In Sec. IV, we give our summary.

II. THE NUCLEON COALESCENCE MODEL

In this section we briefly introduce the nucleon coalescence model, which is used to deal with the formation of light (anti-) nuclei. This model has been successfully used to explain nontrivial behaviors of the coalescence factor measured in different collision systems at the CERN Large Hadron Collider [49].

We start from a hadronic system produced at the final stage of the evolution of high energy collisions and suppose light nuclei are formed via the nucleon coalescence. The three-dimensional momentum distribution of the produced deuterons $f_d(\mathbf{p})$ and that of tritons $f_t(\mathbf{p})$ are given by

$$f_d(\mathbf{p}) = N_{pn} \int d\mathbf{x}_1 d\mathbf{x}_2 d\mathbf{p}_1 d\mathbf{p}_2 f_{pn}^{(n)}(\mathbf{x}_1, \mathbf{x}_2; \mathbf{p}_1, \mathbf{p}_2) \times \mathcal{R}_d(\mathbf{x}_1, \mathbf{x}_2; \mathbf{p}_1, \mathbf{p}_2, \mathbf{p}), \quad (1)$$

$$f_t(\mathbf{p}) = N_{pnn} \int d\mathbf{x}_1 d\mathbf{x}_2 d\mathbf{x}_3 d\mathbf{p}_1 d\mathbf{p}_2 d\mathbf{p}_3 \times f_{pnn}^{(n)}(\mathbf{x}_1, \mathbf{x}_2, \mathbf{x}_3; \mathbf{p}_1, \mathbf{p}_2, \mathbf{p}_3) \times \mathcal{R}_t(\mathbf{x}_1, \mathbf{x}_2, \mathbf{x}_3; \mathbf{p}_1, \mathbf{p}_2, \mathbf{p}_3, \mathbf{p}), \quad (2)$$

where $f_{pn}^{(n)}(\mathbf{x}_1, \mathbf{x}_2; \mathbf{p}_1, \mathbf{p}_2)$ and $f_{pnn}^{(n)}(\mathbf{x}_1, \mathbf{x}_2, \mathbf{x}_3; \mathbf{p}_1, \mathbf{p}_2, \mathbf{p}_3)$ are normalized two- and three-nucleon joint coordinate-momentum distributions, respectively; $N_{pn} = N_p N_n$ is the number of all possible pn pairs and $N_{pnn} = N_p N_n (N_n - 1)$ is that of all possible pnn clusters; N_p is the number of protons and N_n is that of neutrons in the considered hadronic system. $\mathcal{R}_d(\mathbf{x}_1, \mathbf{x}_2; \mathbf{p}_1, \mathbf{p}_2, \mathbf{p})$ and $\mathcal{R}_t(\mathbf{x}_1, \mathbf{x}_2, \mathbf{x}_3; \mathbf{p}_1, \mathbf{p}_2, \mathbf{p}_3, \mathbf{p})$ are kernel functions. Here, and from now on, we use bold symbols to denote three-dimensional coordinates and momenta.

Kernel functions $\mathcal{R}_d(\mathbf{x}_1, \mathbf{x}_2; \mathbf{p}_1, \mathbf{p}_2, \mathbf{p})$ and $\mathcal{R}_t(\mathbf{x}_1, \mathbf{x}_2, \mathbf{x}_3; \mathbf{p}_1, \mathbf{p}_2, \mathbf{p}_3, \mathbf{p})$ carry the kinetic and dynamical information of the nucleons recombining into light nuclei, and their precise expressions should be constrained by such as the momentum conservation, constraints due to intrinsic quantum numbers, e.g., spin, and so on [50]. To take these constraints into account explicitly, we rewrite them in the following forms:

$$\mathcal{R}_d(\mathbf{x}_1, \mathbf{x}_2; \mathbf{p}_1, \mathbf{p}_2, \mathbf{p}) = g_d \mathcal{R}_d^{(x,p)}(\mathbf{x}_1, \mathbf{x}_2; \mathbf{p}_1, \mathbf{p}_2) \delta\left(\sum_{i=1}^2 \mathbf{p}_i - \mathbf{p}\right), \quad (3)$$

$$\mathcal{R}_t(\mathbf{x}_1, \mathbf{x}_2, \mathbf{x}_3; \mathbf{p}_1, \mathbf{p}_2, \mathbf{p}_3, \mathbf{p}) = g_t \times \mathcal{R}_t^{(x,p)}(\mathbf{x}_1, \mathbf{x}_2, \mathbf{x}_3; \mathbf{p}_1, \mathbf{p}_2, \mathbf{p}_3) \delta\left(\sum_{i=1}^3 \mathbf{p}_i - \mathbf{p}\right), \quad (4)$$

where the spin degeneracy factors $g_d = 3/4$ and $g_t = 1/4$. The Dirac δ functions guarantee the momentum conservation in the coalescence. The remaining $\mathcal{R}_d^{(x,p)}(\mathbf{x}_1, \mathbf{x}_2; \mathbf{p}_1, \mathbf{p}_2)$ can be solved from the Wigner transformation once the wave functions of the light nuclei are given with the instantaneous coalescence approximation. They are as follows:

$$\mathcal{R}_d^{(x,p)}(\mathbf{x}_1, \mathbf{x}_2; \mathbf{p}_1, \mathbf{p}_2) = 8e^{-\frac{(\alpha'_1 - \alpha'_2)^2}{\sigma_d^2}} e^{-\frac{\sigma_d^2(\mathbf{p}'_1 - \mathbf{p}'_2)^2}{4n^2 c^2}}, \quad (5)$$

$$\mathcal{R}_t^{(x,p)}(\mathbf{x}_1, \mathbf{x}_2, \mathbf{x}_3; \mathbf{p}_1, \mathbf{p}_2, \mathbf{p}_3) = 8^2 e^{-\frac{(\alpha'_1 - \alpha'_2)^2}{2\sigma_t^2}} e^{-\frac{(\alpha'_1 + \alpha'_2 - 2\alpha'_3)^2}{6\sigma_t^2}} \times e^{-\frac{\sigma_t^2(\mathbf{p}'_1 - \mathbf{p}'_2)^2}{2n^2 c^2}} e^{-\frac{\sigma_t^2(\mathbf{p}'_1 + \mathbf{p}'_2 - 2\mathbf{p}'_3)^2}{6n^2 c^2}}, \quad (6)$$

as we adopt the wave function of a spherical harmonic oscillator as in Refs. [51,52]. The superscript “ x,p ” in the coordinate or momentum variable denotes the coordinate or momentum

of the nucleon in the rest frame of the pn pair or pnn cluster. The width parameter $\sigma_d = \sqrt{\frac{8}{3}}R_d$ and $\sigma_t = R_t$, where R_d and R_t are the root-mean-square radius of the deuteron and that of the triton, respectively. The factor $\hbar c$ comes from the used GeV fm unit, and it is 0.197 GeV fm.

The normalized nucleon joint distributions $f_{pn}^{(n)}(\mathbf{x}_1, \mathbf{x}_2; \mathbf{p}_1, \mathbf{p}_2)$ and $f_{pnn}^{(n)}(\mathbf{x}_1, \mathbf{x}_2, \mathbf{x}_3; \mathbf{p}_1, \mathbf{p}_2, \mathbf{p}_3)$ are generally coordinate and momentum coupled, especially in central heavy-ion collisions with relatively high collision energies where the collective expansion long exists. The coupling intensities and its specific forms are probably different in different collision energies and different collision centralities. In this article, we try our best to derive production formulas analytically and present centrality and collision energy dependencies of light nuclei more intuitively at RHIC beam energy scan energies, so we consider a simple case that they are coordinate and momentum factorized, i.e.,

$$f_{pn}^{(n)}(\mathbf{x}_1, \mathbf{x}_2; \mathbf{p}_1, \mathbf{p}_2) = f_{pn}^{(n)}(\mathbf{x}_1, \mathbf{x}_2) f_{pn}^{(n)}(\mathbf{p}_1, \mathbf{p}_2), \quad (7)$$

$$f_{pnn}^{(n)}(\mathbf{x}_1, \mathbf{x}_2, \mathbf{x}_3; \mathbf{p}_1, \mathbf{p}_2, \mathbf{p}_3) = f_{pnn}^{(n)}(\mathbf{x}_1, \mathbf{x}_2, \mathbf{x}_3) \times f_{pnn}^{(n)}(\mathbf{p}_1, \mathbf{p}_2, \mathbf{p}_3). \quad (8)$$

Substituting Eqs. (3)–(8) into Eqs. (1) and (2), we have

$$f_d(\mathbf{p}) = g_d N_{pn} \int d\mathbf{x}_1 d\mathbf{x}_2 f_{pn}^{(n)}(\mathbf{x}_1, \mathbf{x}_2) 8e^{-\frac{(\mathbf{x}'_1 - \mathbf{x}'_2)^2}{\sigma_d^2}} \times \int d\mathbf{p}_1 d\mathbf{p}_2 f_{pn}^{(n)}(\mathbf{p}_1, \mathbf{p}_2) e^{-\frac{\sigma_d^2(\mathbf{p}'_1 - \mathbf{p}'_2)^2}{4\hbar^2 c^2}} \delta\left(\sum_{i=1}^2 \mathbf{p}_i - \mathbf{p}\right), \quad (9)$$

$$f_t(\mathbf{p}) = g_t N_{pnn} \int d\mathbf{x}_1 d\mathbf{x}_2 d\mathbf{x}_3 f_{pnn}^{(n)}(\mathbf{x}_1, \mathbf{x}_2, \mathbf{x}_3) 8^2 \times e^{-\frac{(\mathbf{x}'_1 - \mathbf{x}'_2)^2}{2\sigma_t^2}} e^{-\frac{(\mathbf{x}'_1 + \mathbf{x}'_2 - 2\mathbf{x}'_3)^2}{6\sigma_t^2}} \times \int d\mathbf{p}_1 d\mathbf{p}_2 d\mathbf{p}_3 f_{pnn}^{(n)}(\mathbf{p}_1, \mathbf{p}_2, \mathbf{p}_3) \times e^{-\frac{\sigma_t^2(\mathbf{p}'_1 - \mathbf{p}'_2)^2}{2\hbar^2 c^2}} e^{-\frac{\sigma_t^2(\mathbf{p}'_1 + \mathbf{p}'_2 - 2\mathbf{p}'_3)^2}{6\hbar^2 c^2}} \delta\left(\sum_{i=1}^3 \mathbf{p}_i - \mathbf{p}\right). \quad (10)$$

Equations (9) and (10) show that we can calculate momentum distributions of different light nuclei by integrating coordinates and momenta of nucleons, respectively.

We use \mathcal{A}_d and \mathcal{A}_t to denote the coordinate integral parts in Eqs. (9) and (10) as

$$\mathcal{A}_d = 8 \int d\mathbf{x}_1 d\mathbf{x}_2 f_{pn}^{(n)}(\mathbf{x}_1, \mathbf{x}_2) e^{-\frac{(\mathbf{x}'_1 - \mathbf{x}'_2)^2}{\sigma_d^2}}, \quad (11)$$

$$\mathcal{A}_t = 8^2 \int d\mathbf{x}_1 d\mathbf{x}_2 d\mathbf{x}_3 f_{pnn}^{(n)}(\mathbf{x}_1, \mathbf{x}_2, \mathbf{x}_3) \times e^{-\frac{(\mathbf{x}'_1 - \mathbf{x}'_2)^2}{2\sigma_t^2}} e^{-\frac{(\mathbf{x}'_1 + \mathbf{x}'_2 - 2\mathbf{x}'_3)^2}{6\sigma_t^2}}, \quad (12)$$

and use $\mathcal{M}_d(\mathbf{p})$ and $\mathcal{M}_t(\mathbf{p})$ to denote the momentum integral parts as

$$\mathcal{M}_d(\mathbf{p}) = \int d\mathbf{p}_1 d\mathbf{p}_2 f_{pn}^{(n)}(\mathbf{p}_1, \mathbf{p}_2) e^{-\frac{\sigma_d^2(\mathbf{p}'_1 - \mathbf{p}'_2)^2}{4\hbar^2 c^2}} \delta\left(\sum_{i=1}^2 \mathbf{p}_i - \mathbf{p}\right), \quad (13)$$

$$\mathcal{M}_t(\mathbf{p}) = \int d\mathbf{p}_1 d\mathbf{p}_2 d\mathbf{p}_3 f_{pnn}^{(n)}(\mathbf{p}_1, \mathbf{p}_2, \mathbf{p}_3) \times e^{-\frac{\sigma_t^2(\mathbf{p}'_1 - \mathbf{p}'_2)^2}{2\hbar^2 c^2}} e^{-\frac{\sigma_t^2(\mathbf{p}'_1 + \mathbf{p}'_2 - 2\mathbf{p}'_3)^2}{6\hbar^2 c^2}} \delta\left(\sum_{i=1}^3 \mathbf{p}_i - \mathbf{p}\right). \quad (14)$$

So we get

$$f_d(\mathbf{p}) = g_d N_{pn} \mathcal{A}_d \mathcal{M}_d(\mathbf{p}), \quad (15)$$

$$f_t(\mathbf{p}) = g_t N_{pnn} \mathcal{A}_t \mathcal{M}_t(\mathbf{p}). \quad (16)$$

\mathcal{A}_d stands for the probability of a pn pair satisfying the coordinate requirement to recombine into a deuteron-like molecular state, and $\mathcal{M}_d(\mathbf{p})$ stands for the probability of a pn pair satisfying the momentum requirement to recombine into a deuteron-like molecular state with momentum \mathbf{p} . The similar case holds for \mathcal{A}_t and $\mathcal{M}_t(\mathbf{p})$.

Changing coordinate integral variables in Eq. (11) to be $\mathbf{X}_C = \frac{\mathbf{x}_1 + \mathbf{x}_2}{2}$ and $\mathbf{r} = \mathbf{x}_1 - \mathbf{x}_2$, and those in Eq. (12) to be $\mathbf{Y}_C = (\mathbf{x}_1 + \mathbf{x}_2 + \mathbf{x}_3)/\sqrt{3}$, $\mathbf{r}_1 = (\mathbf{x}_1 - \mathbf{x}_2)/\sqrt{2}$, and $\mathbf{r}_2 = (\mathbf{x}_1 + \mathbf{x}_2 - 2\mathbf{x}_3)/\sqrt{6}$, we have

$$\mathcal{A}_d = 8 \int d\mathbf{X}_C d\mathbf{r} f_{pn}^{(n)}(\mathbf{X}_C, \mathbf{r}) e^{-\frac{\mathbf{r}^2}{\sigma_d^2}}, \quad (17)$$

$$\mathcal{A}_t = 8^2 \int d\mathbf{Y}_C d\mathbf{r}_1 d\mathbf{r}_2 f_{pnn}^{(n)}(\mathbf{Y}_C, \mathbf{r}_1, \mathbf{r}_2) e^{-\frac{(\mathbf{r}'_1)^2 + (\mathbf{r}'_2)^2}{\sigma_t^2}}. \quad (18)$$

We further assume the coordinate joint distributions are coordinate variable factorized, i.e., $f_{pn}^{(n)}(\mathbf{X}_C, \mathbf{r}) = f_{pn}^{(n)}(\mathbf{X}_C) f_{pn}^{(n)}(\mathbf{r})$ and $f_{pnn}^{(n)}(\mathbf{Y}_C, \mathbf{r}_1, \mathbf{r}_2) = f_{pnn}^{(n)}(\mathbf{Y}_C) f_{pnn}^{(n)}(\mathbf{r}_1) f_{pnn}^{(n)}(\mathbf{r}_2)$. Then we have

$$\mathcal{A}_d = 8 \int d\mathbf{r} f_{pn}^{(n)}(\mathbf{r}) e^{-\frac{\mathbf{r}^2}{\sigma_d^2}}, \quad (19)$$

$$\mathcal{A}_t = 8^2 \int d\mathbf{r}_1 d\mathbf{r}_2 f_{pnn}^{(n)}(\mathbf{r}_1) f_{pnn}^{(n)}(\mathbf{r}_2) e^{-\frac{(\mathbf{r}'_1)^2 + (\mathbf{r}'_2)^2}{\sigma_t^2}}. \quad (20)$$

As in Refs. [49,53], we adopt $f_{pn}^{(n)}(\mathbf{r}) = \frac{1}{(\pi C R_f^2)^{1.5}} e^{-\frac{\mathbf{r}^2}{C R_f^2}}$ and $f_{pnn}^{(n)}(\mathbf{r}_1) = \frac{1}{(\pi C_1 R_f^2)^{1.5}} e^{-\frac{\mathbf{r}_1^2}{C_1 R_f^2}}$, $f_{pnn}^{(n)}(\mathbf{r}_2) = \frac{1}{(\pi C_2 R_f^2)^{1.5}} e^{-\frac{\mathbf{r}_2^2}{C_2 R_f^2}}$, where R_f is the effective radius of the source system at the light nuclei freeze-out and C , C_1 , and C_2 are distribution width parameters. Considering relations between \mathbf{r} , \mathbf{r}_1 , and \mathbf{r}_2 with \mathbf{x}_1 , \mathbf{x}_2 , and \mathbf{x}_3 , C_1 should be equal to $C/2$, and C_2 should be equal to $2C/3$. So there is only one distribution width parameter C to be determined. In this article we set it to be 4, the same as that in Refs. [49,53].

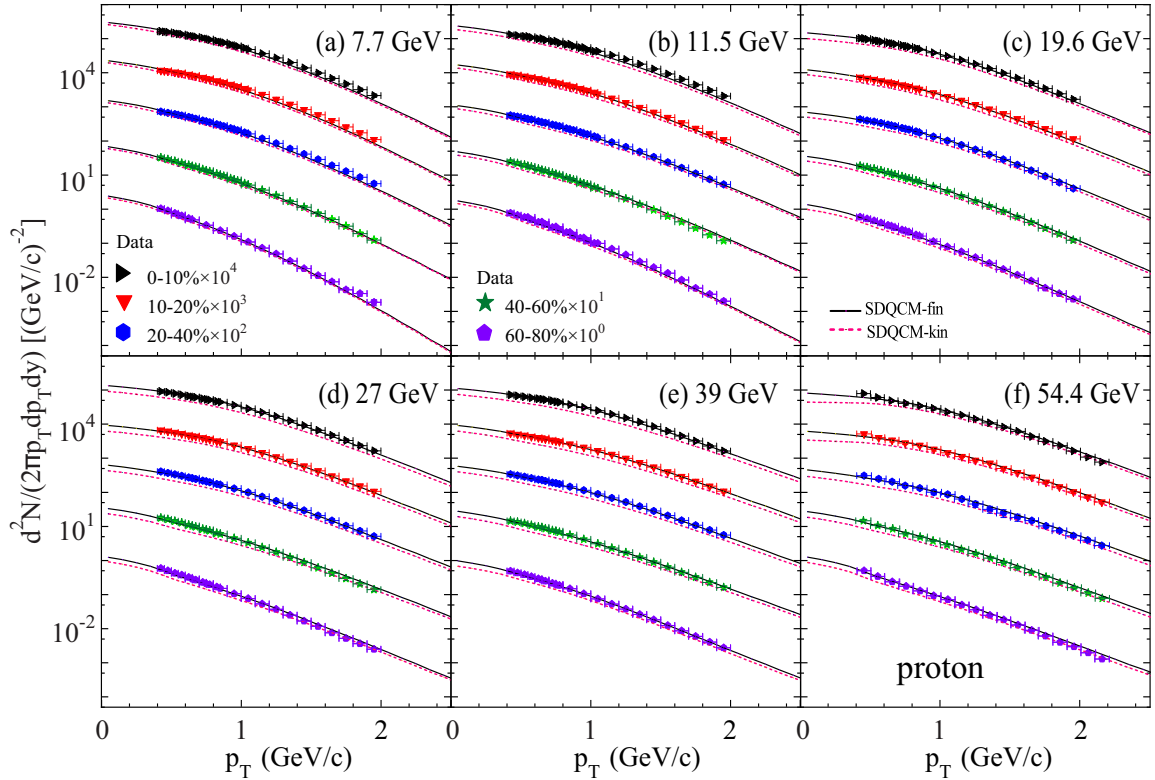


FIG. 1. Invariant p_T spectra of protons at midrapidity in Au-Au collisions at $\sqrt{s_{NN}} = 7.7, 11.5, 19.6, 27, 39, 54.4$ GeV in centralities 0–10 %, 10–20 %, 20–40 %, 40–60 %, and 60–80 %. Filled symbols are experimental data from the STAR Collaboration [43,56]. Solid lines are the results of final state protons and dashed lines are those at the kinetic freeze-out calculated by the SDQCM.

Considering instantaneous coalescence in the rest frame of the $pnpair$ or pnn cluster, i.e., $\Delta t' = 0$, we get

$$\mathbf{r} = \mathbf{r}' + (\gamma - 1) \frac{\mathbf{r}' \boldsymbol{\beta}}{\beta^2}. \quad (21)$$

Substituting the above equation into Eqs. (19) and (20) and integrating from relative coordinate variables, we can obtain

$$\mathcal{A}_d = \frac{8\sigma_d^3}{(CR_f^2 + \sigma_d^2)\sqrt{C(R_f/\gamma)^2 + \sigma_d^2}}, \quad (22)$$

$$\begin{aligned} \mathcal{A}_t &= \frac{8\sigma_t^3}{(\frac{C}{2}R_f^2 + \sigma_t^2)\sqrt{\frac{C}{2}(R_f/\gamma)^2 + \sigma_t^2}} \\ &\times \frac{8\sigma_t^3}{(\frac{2C}{3}R_f^2 + \sigma_t^2)\sqrt{\frac{2C}{3}(R_f/\gamma)^2 + \sigma_t^2}}. \end{aligned} \quad (23)$$

Recalling that $\sigma_d = \sqrt{\frac{8}{3}}R_d$ and $\sigma_t = R_t$, where the root-mean-square charge radius of the deuteron $R_d = 2.1421$ fm and that of the t $R_t = 1.7591$ fm [54], we see that the gaussian width values $2\hbar c/\sigma_d$, $\sqrt{2}\hbar c/\sigma_t$, and $\sqrt{6}\hbar c/\sigma_t$ in Eqs. (13) and (14) are quite small. So we can mathematically approximate the gaussian form of the kernel function $e^{-(\Delta\mathbf{p}')^2/\epsilon^2}$ as $(\sqrt{\pi}\epsilon)^3\delta(\Delta\mathbf{p}')$, where ϵ is a small quantity. Then we

immediately obtain

$$\begin{aligned} \mathcal{M}_d(\mathbf{p}) &= \left(\frac{2\hbar c}{\sigma_d}\sqrt{\pi}\right)^3 \int d\mathbf{p}_1 d\mathbf{p}_2 f_{pn}^{(n)}(\mathbf{p}_1, \mathbf{p}_2) \delta(\mathbf{p}'_1 - \mathbf{p}'_2) \\ &\times \delta\left(\sum_{i=1}^2 \mathbf{p}_i - \mathbf{p}_d\right) \\ &= \left(\frac{2\hbar c}{\sigma_d}\sqrt{\pi}\right)^3 \int d\mathbf{p}_1 d\mathbf{p}_2 f_{pn}^{(n)}(\mathbf{p}_1, \mathbf{p}_2) \gamma \delta(\mathbf{p}_1 - \mathbf{p}_2) \\ &\times \delta\left(\sum_{i=1}^2 \mathbf{p}_i - \mathbf{p}_d\right) \\ &= \left(\frac{\hbar c}{\sigma_d}\sqrt{\pi}\right)^3 \gamma f_{pn}^{(n)}\left(\frac{\mathbf{p}}{2}, \frac{\mathbf{p}}{2}\right), \end{aligned} \quad (24)$$

where γ comes from $\Delta\mathbf{p}' = \frac{1}{\gamma}\Delta\mathbf{p}$. Similarly we get

$$\mathcal{M}_t(\mathbf{p}) = \left(\frac{\pi\hbar^2 c^2}{\sqrt{3}\sigma_t^2}\right)^3 \gamma^2 f_{pnn}^{(n)}\left(\frac{\mathbf{p}}{3}, \frac{\mathbf{p}}{3}, \frac{\mathbf{p}}{3}\right). \quad (25)$$

The robustness of the above δ function approximation has been checked in our recent work [49].

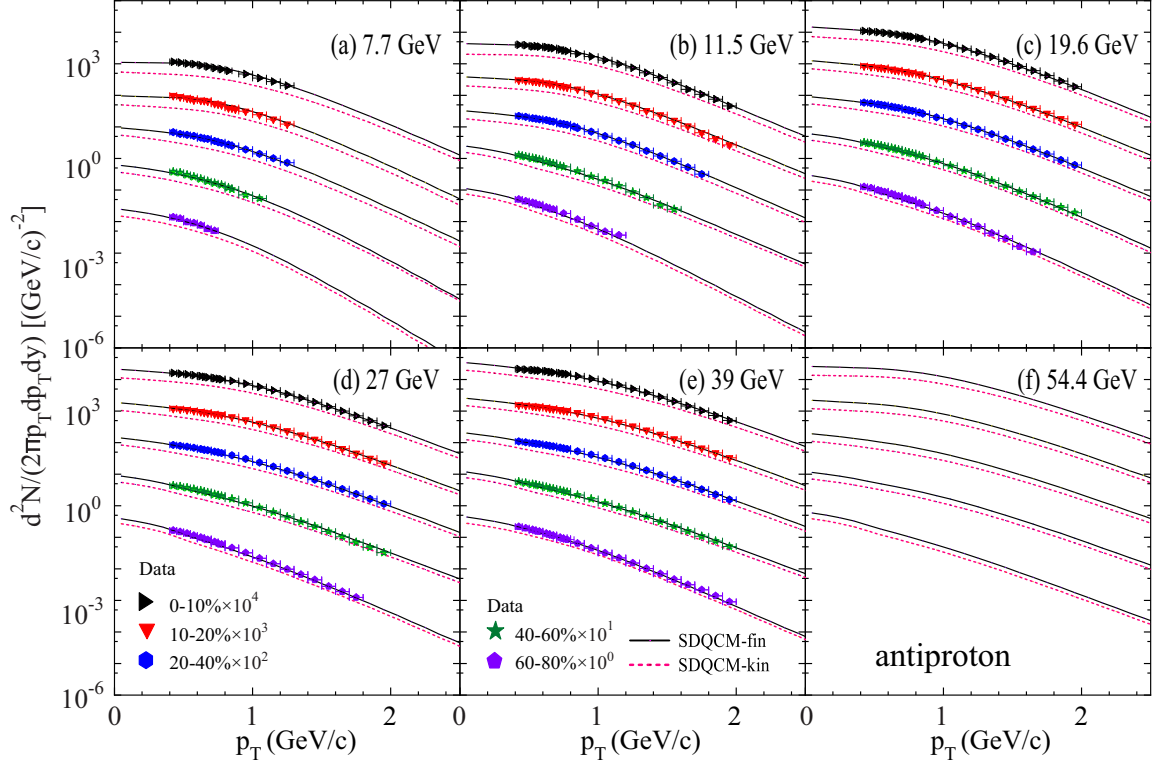


FIG. 2. Invariant p_T spectra of antiprotons at midrapidity in Au-Au collisions at $\sqrt{s_{NN}} = 7.7, 11.5, 19.6, 27, 39, 54.4$ GeV in centralities 0–10 %, 10–20 %, 20–40 %, 40–60 %, and 60–80 %. Filled symbols are experimental data from the STAR Collaboration [43,56]. Solid lines are the results of final state antiprotons and dashed lines are those at the kinetic freeze-out calculated by the SDQCM.

Substituting Eqs. (22)–(25) into Eqs. (15) and (16), and ignoring correlations between protons and neutrons, we finally have the momentum distributions of light nuclei as

$$f_d(\mathbf{p}) = \frac{8(\sqrt{\pi}\hbar c)^3 g_d \gamma}{(CR_f^2 + \sigma_d^2)\sqrt{C(R_f/\gamma)^2 + \sigma_d^2}} f_p\left(\frac{\mathbf{p}}{2}\right) f_n\left(\frac{\mathbf{p}}{2}\right), \quad (26)$$

$$f_i(\mathbf{p}) = \frac{8^2(\pi\hbar^2 c^2)^3 g_i \gamma^2}{3\sqrt{3}(\frac{C}{2}R_f^2 + \sigma_i^2)\sqrt{\frac{C}{2}(R_f/\gamma)^2 + \sigma_i^2}} \times \frac{1}{(\frac{2C}{3}R_f^2 + \sigma_i^2)\sqrt{\frac{2C}{3}(R_f/\gamma)^2 + \sigma_i^2}} f_p\left(\frac{\mathbf{p}}{3}\right) \times f_n\left(\frac{\mathbf{p}}{3}\right) f_n\left(\frac{\mathbf{p}}{3}\right). \quad (27)$$

From Eqs. (26) and (27), we can get the Lorentz invariant momentum distributions of light nuclei. We denote the invariant distribution $\frac{d^2N}{2\pi p_T dp_T dy}$ with f^{inv} and at the midrapidity $y = 0$ we have

$$f_d^{inv}(p_T) = \frac{32(\sqrt{\pi}\hbar c)^3 g_d}{m_d(CR_f^2 + \sigma_d^2)\sqrt{C(R_f/\gamma)^2 + \sigma_d^2}} \times f_p^{inv}\left(\frac{p_T}{2}\right) f_n^{inv}\left(\frac{p_T}{2}\right), \quad (28)$$

$$f_t^{inv}(p_T) = \frac{192\sqrt{3}(\pi\hbar^2 c^2)^3 g_t}{m_t^2(\frac{C}{2}R_f^2 + \sigma_t^2)\sqrt{\frac{C}{2}(R_f/\gamma)^2 + \sigma_t^2}(\frac{2C}{3}R_f^2 + \sigma_t^2)} \times \frac{1}{\sqrt{\frac{2C}{3}(R_f/\gamma)^2 + \sigma_t^2}} f_p^{inv}\left(\frac{p_T}{3}\right) \times f_n^{inv}\left(\frac{p_T}{3}\right) f_n^{inv}\left(\frac{p_T}{3}\right). \quad (29)$$

Equations (28) and (29) show relationships of light nuclei with primordial nucleons in momentum space in the laboratory frame. They can be directly used to calculate the yields and p_T spectra of light nuclei measured extensively as long as the nucleon Lorentz invariant momentum distributions are given.

III. RESULTS AND DISCUSSIONS

In this section, we apply the deduced results in Sec. II to the midrapidity region of Au-Au collisions at the RHIC energies to study production characteristics of light (anti-)nuclei from the nucleon coalescence. First we give the p_T distributions of final-state (anti-)protons and those at the kinetic freeze-out calculated by the SDQCM [48]. Then we present the results of p_T distributions of light nuclei and antinuclei. Finally we show yields and several interesting yield ratios of different light (anti-)nuclei d/p , \bar{d}/\bar{p} , t/p , \bar{t}/\bar{p} , d/p^2 , \bar{d}/\bar{p}^2 , tp/d^2 , etc., and discuss their properties as functions of the collision energy and the collision centrality.

TABLE I. Yield densities dN/dy of protons and antiprotons at midrapidity in Au-Au collisions at $\sqrt{s_{NN}} = 7.7, 11.5, 19.6, 27, 39, 54.4$ GeV. Data in the third and sixth columns are from Ref. [56]. QCM-fin at $\sqrt{s_{NN}} = 54.4$ GeV denotes final state protons and antiprotons calculated by the SDQCM. QCM-cor in the fourth and seventh columns denotes (anti-) protons corrected from weak decays calculated by the SDQCM. Weak decay contribution (WDC) ratio is evaluated and the results are in fifth and eighth columns.

$\sqrt{s_{NN}}$	Centrality	p			\bar{p}		
		data	QCM-cor	WDC	data	QCM-cor	WDC
7.7 GeV	0–10 %	50.2 ± 5.6	41.0	18.2%	0.36 ± 0.05	0.17	52.5%
	10–20 %	33.4 ± 3.7	27.5	17.5%	0.26 ± 0.03	0.13	50.7%
	20–40 %	19.5 ± 2.2	16.3	16.5%	0.17 ± 0.02	0.09	46.2%
	40–60 %	7.4 ± 0.8	6.3	14.9%	0.08 ± 0.01	0.05	40.0%
	60–80 %	2.1 ± 0.3	1.8	12.9%	0.026 ± 0.003	0.016	36.7%
11.5 GeV	0–10 %	39.6 ± 4.8	30.2	23.7%	1.4 ± 0.2	0.7	48.4%
	10–20 %	26.1 ± 3.1	20.1	23.0%	0.9 ± 0.1	0.5	46.7%
	20–40 %	14.8 ± 1.8	11.5	22.3%	0.6 ± 0.1	0.3	44.4%
	40–60 %	5.8 ± 0.7	4.5	20.9%	0.27 ± 0.04	0.17	38.6%
	60–80 %	1.6 ± 0.2	1.3	17.7%	0.10 ± 0.02	0.06	33.5%
19.6 GeV	0–10 %	31.8 ± 4.2	22.1	30.3%	3.8 ± 0.5	2.1	45.3%
	10–20 %	21.9 ± 2.9	15.5	29.5%	2.7 ± 0.4	1.5	44.5%
	20–40 %	11.9 ± 1.6	8.4	28.9%	1.7 ± 0.3	1.0	42.2%
	40–60 %	4.6 ± 0.6	3.3	26.9%	0.8 ± 0.1	0.5	37.4%
	60–80 %	1.3 ± 0.2	1.0	25.0%	0.27 ± 0.04	0.18	33.2%
27 GeV	0–10 %	29.1 ± 3.5	19.4	33.3%	5.6 ± 0.7	3.2	43.2%
	10–20 %	19.4 ± 2.3	13.3	31.2%	4.0 ± 0.5	2.3	41.7%
	20–40 %	10.9 ± 1.3	7.6	30.8%	2.5 ± 0.3	1.5	40.1%
	40–60 %	4.4 ± 0.6	3.1	29.6%	1.1 ± 0.2	0.7	36.7%
	60–80 %	1.3 ± 0.2	0.2	25.4%	0.36 ± 0.04	0.25	31.4%
39 GeV	0–10 %	24.6 ± 2.7	16.2	34.1%	8.0 ± 1.0	4.6	42.3%
	10–20 %	17.3 ± 1.9	11.5	33.5%	5.4 ± 0.7	3.2	41.1%
	20–40 %	9.9 ± 1.1	6.7	32.2%	3.4 ± 0.4	2.1	39.3%
	40–60 %	3.9 ± 0.4	2.7	30.2%	1.5 ± 0.2	1.0	35.2%
	60–80 %	1.1 ± 0.2	0.8	27.5%	0.49 ± 0.06	0.33	32.2%
54.4 GeV		QCM-fin			QCM-fin		
	0–10 %	23.6	15.3	35.2%	9.9	5.8	41.3%
	10–20 %	16.2	10.5	34.8%	6.8	4.0	41.0%
	20–40 %	8.7	5.7	34.7%	4.1	2.5	39.8%
	40–60 %	3.5	2.4	30.8%	1.8	1.2	35.3%
	60–80 %	1.1	0.7	29.7%	0.6	0.4	32.8%

A. p_T spectra of protons and antiprotons

The (anti-)nucleon p_T distributions are necessary for computing p_T distributions of light (anti-)nuclei in our method. We use SDQCM to obtain invariant p_T distributions of protons and antiprotons at the final state as well as those at the kinetic freeze-out. The detailed calculations for hadron production at the RHIC beam energy scan with the SDQCM can be found in our previous works [47,48,55].

Figures 1 and 2 show the invariant p_T spectra of protons and antiprotons at midrapidity in Au-Au collisions at $\sqrt{s_{NN}} = 7.7, 11.5, 19.6, 27, 39, 54.4$ GeV in centralities 0–10 %, 10–20 %, 20–40 %, 40–60 %, and 60–80 %. Filled symbols are experimental data from the STAR Collaboration in Refs. [43,56]. Solid lines are the results of final state protons calculated by the SDQCM, which describe the data well. Dashed lines are the results of (anti-)protons at the kinetic freeze-out, which are just those we need for computing the production of light (anti-)nuclei. The surplus of solid lines

compared to dashed lines comes from the weak decays of hyperons after the kinetic freeze-out.

To see weak decay contaminations more clearly, we show the yield density dN/dy of protons and that of antiprotons for final state ones and those corrected weak decays in Table I. The contamination ratio from weak decays (WDC) is evaluated and the results are in fifth and eighth columns, from which one can see that the weak decay corrections exhibit explicit energy and centrality dependencies. The contamination from weak decays for both protons and antiprotons becomes larger in more central collisions at the same collision energy because strangeness production is enhanced from peripheral to central collisions. At the same centrality bin, WDC for protons become larger while for antiprotons they become smaller as the function of the colliding energy. This is due to more newborn baryons and slightly decreasing strangeness production with the increasing energy.

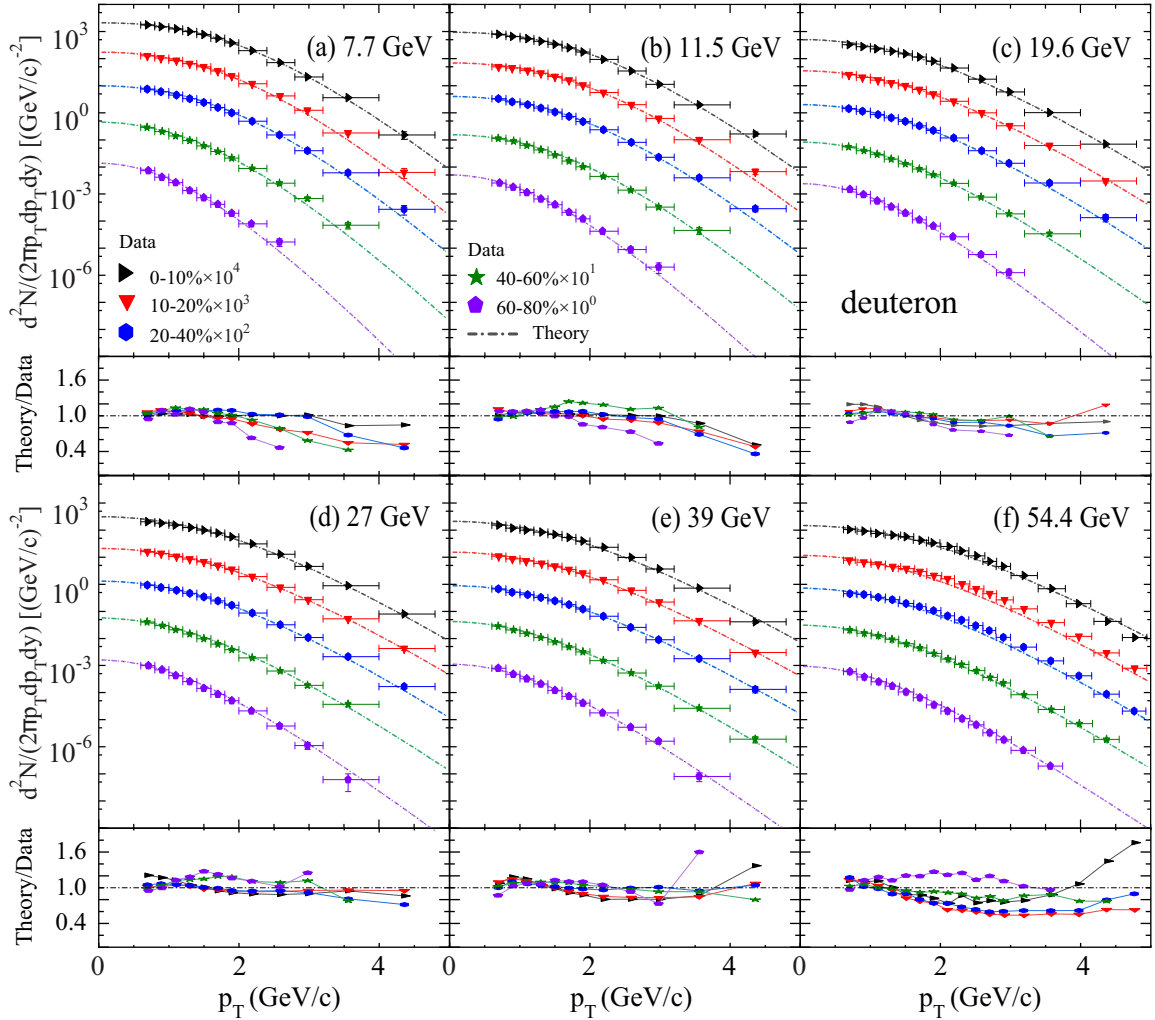


FIG. 3. Invariant p_T spectra of deuterons at midrapidity in Au-Au collisions in different centralities at $\sqrt{s_{NN}} = 7.7, 11.5, 19.6, 27, 39, 54.4$ GeV. Filled symbols are the data [43,45]. Dashed-dotted lines are our theoretical results. Spectra for different centralities are scaled by different factors for clarity. Theory/data points connected by lines to guide the eye are plotted below each panel.

B. p_T spectra of light nuclei and antinuclei

According to Eqs. (28) and (29), the p_T distributions of deuterons and tritons can be computed with the proton p_T distributions shown in Fig. 1. The isospin symmetry is adopted, i.e., we assume the p_T distribution of the neutron is the same with that of the proton. The effective radius of the hadronic system R_f is characterized by the rapidity density of charged particles dN_{ch}/dy as $R_f = a * (dN_{ch}/dy)^{1/3}$ [57,58], where a is a free parameter. In the current article, $a = 0.58$ for both d and \bar{d} , and $a = 0.55$ for both t and \bar{t} . The slightly lower value of a for t , \bar{t} may indicate their earlier freezeout compared to d , \bar{d} in our model. Values of a we used here are a little larger than those $a = 0.51, 0.43$ for d , ${}^3\text{He}$ in Pb-Pb collisions at the LHC we previously adopted in Ref. [49]. Note that a is fixed by the best reproduction of the experimental data. Considering the error bars of the current data of the charged multiplicity density, the proton yield density, and light nuclei, a for d can fluctuate about 15% and a for ${}^3\text{He}$ can

fluctuate about 14% at LHC. Similar fluctuations for a hold at RHIC. Within these fluctuations, values of a at RHIC and LHC energies are comparable. With the data of dN_{ch}/dy in Ref. [56], we get the value of R_f and then we can compute p_T distributions of d , \bar{d} , t , and \bar{t} .

Figures 3 and 4 show p_T spectra for d and \bar{d} at midrapidity in Au-Au collisions in 0–10%, 10–20%, 20–40%, 40–60%, and 60–80% centralities at $\sqrt{s_{NN}} = 7.7, 11.5, 19.6, 27, 39, 54.4$ GeV. Filled symbols are the data from the STAR Collaboration [43,45]. Dashed-dotted lines are our theoretical results. The spectra for different centralities are scaled by different factors for clarity as shown in the figures. Theory/data points connected by lines to guide the eye are also plotted in linear scale below each panel. From Figs. 3 and 4, one can see that the coalescence model can reproduce the available data for both d and \bar{d} from central to peripheral Au-Au collisions at the beam energy scan energies.

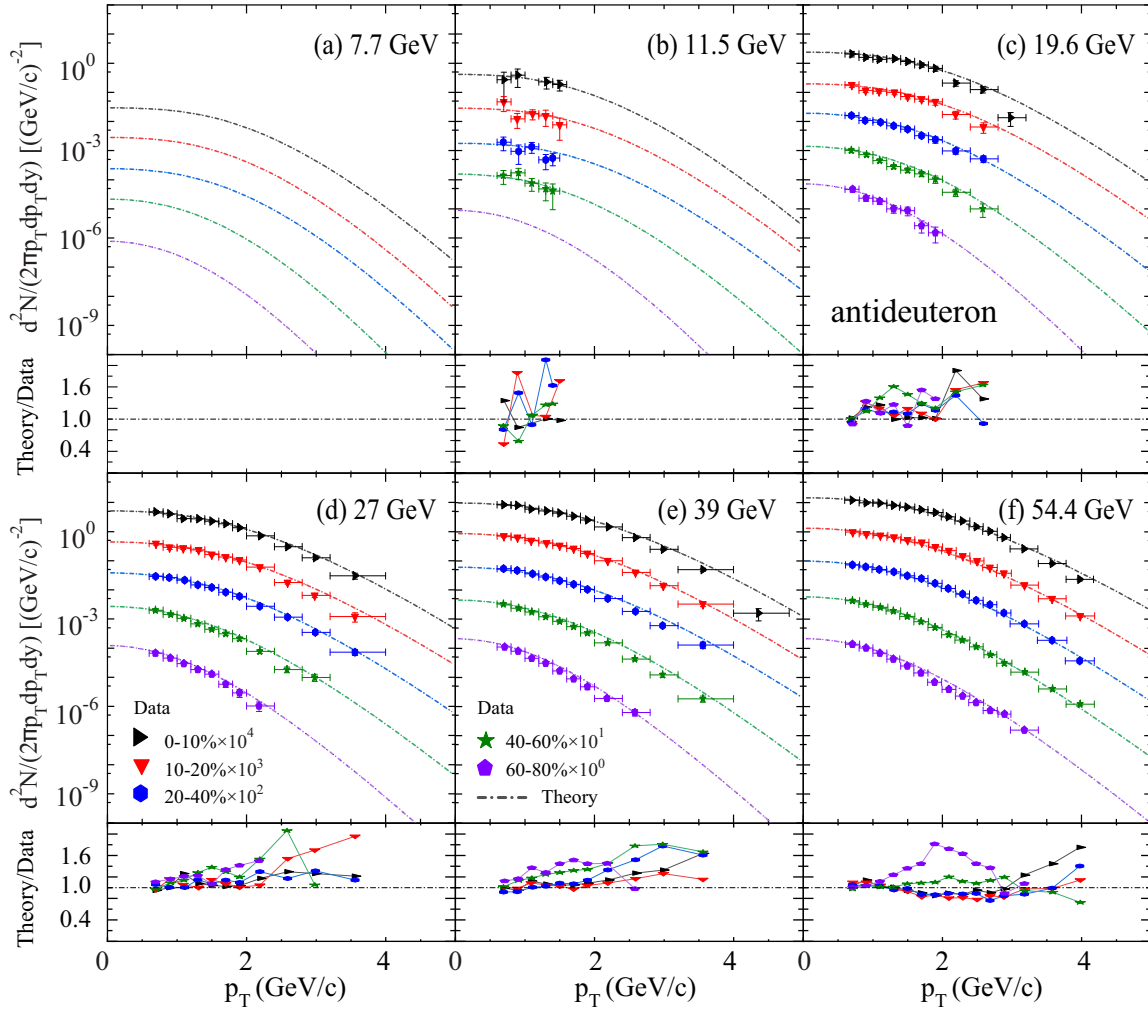


FIG. 4. Invariant p_T spectra of antideuterons at midrapidity in Au-Au collisions in different centralities at $\sqrt{s_{NN}} = 7.7, 11.5, 19.6, 27, 39, 54.4$ GeV. Filled symbols are the data [43,45]. Dashed-dotted lines are our theoretical results. The spectra for different centralities are scaled by different factors for clarity. Theory/data points connected by lines to guide the eye are plotted below each panel.

Figure 5 shows p_T spectra of tritons at midrapidity in Au-Au collisions in 0–10%, 10–20%, 20–40%, and 40–80% centralities at $\sqrt{s_{NN}} = 7.7, 11.5, 19.6, 27, 39, 54.4$ GeV. Filled symbols are the data from STAR Collaboration [43]. Dashed lines are our theoretical results, which agree with the available data. The spectra for different centralities are scaled by different factors for clarity as shown in the figure. Theory/data points connected by lines to guide the eye are also plotted in linear scale below each panel. We also predict the invariant p_T spectra of antitritons and the results are in Fig. 6.

The consistency between the theoretical results from the coalescence model and the data for $d, \bar{d}, t,$ and \bar{t} in Figs. 3–6 show the dominant role of the coalescence mechanism in describing the production of light nuclei and antinuclei at these RHIC energies.

C. Yield densities dN/dy of light nuclei and antinuclei

After integrating over the p_T , we can get the rapidity yield densities of light (anti-)nuclei. Table II shows our results of $d, \bar{d}, t,$ and \bar{t} in Au-Au collisions at midrapidity in different centralities at $\sqrt{s_{NN}} = 7.7, 11.5, 19.6, 27, 39, 54.4$ GeV. Data with errors are from Refs. [43,45]. Our results are consistent with the available data. dN/dy becomes larger for both light nuclei and antinuclei from peripheral to central collisions at the same collision energy. This is due to the more energy deposited in the reaction region in more central collisions. For the same centrality, dN/dy of light nuclei decreases gradually, while for antinuclei it increases with the increasing collision energy. This is related with the net nucleons from the colliding heavy nuclei. It is easier for them to stop in the midrapidity region to form light nuclei in lower collision energies.

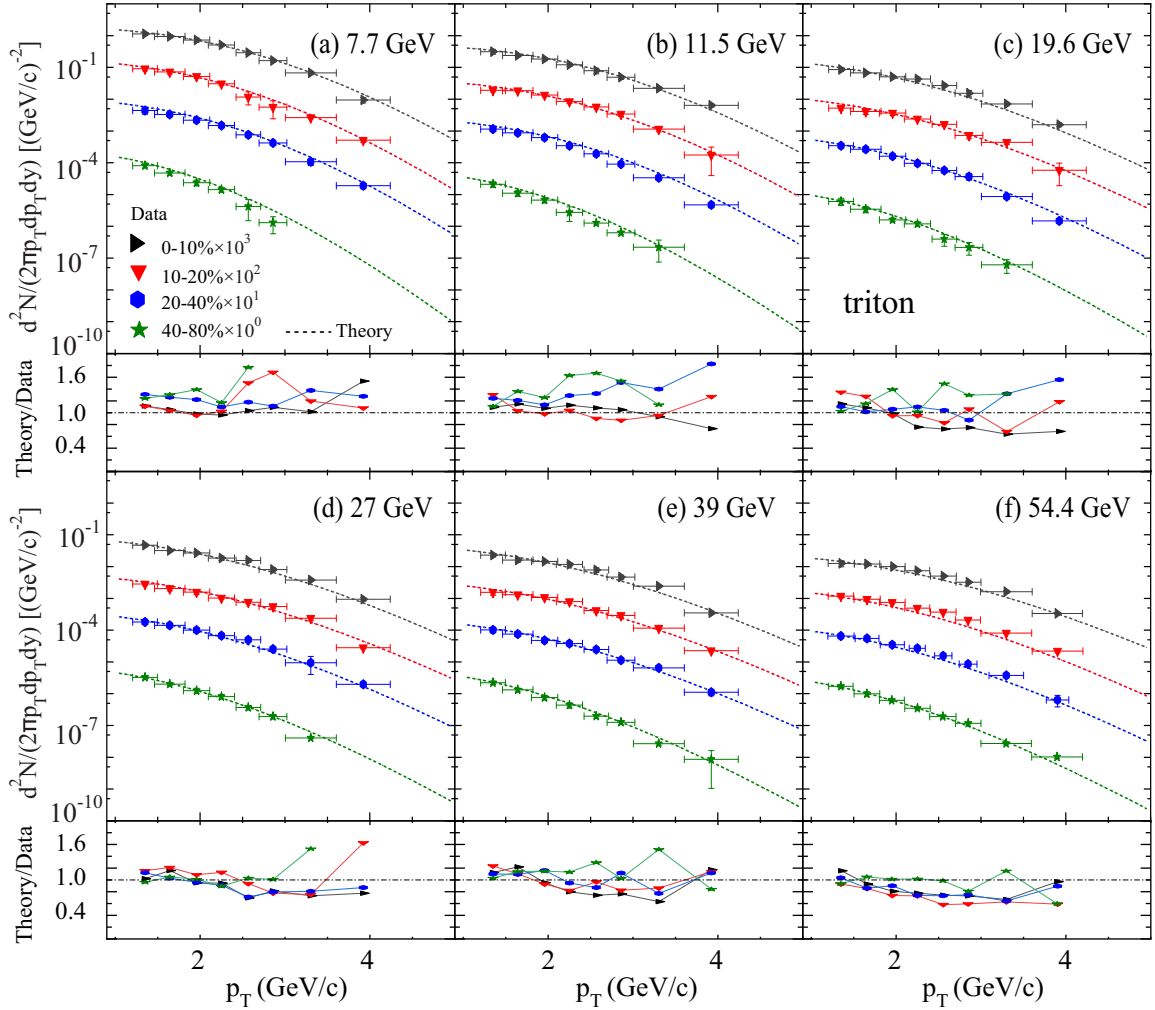


FIG. 5. Invariant p_T spectra of tritons at midrapidity in Au-Au collisions in different centralities at $\sqrt{s_{NN}} = 7.7, 11.5, 19.6, 27, 39, 54.4$ GeV. Filled symbols are the data [43]. Different dashed lines are theoretical results. Spectra in different centralities are scaled by different factors for clarity. Theory/data points connected by lines to guide the eye are plotted below each panel.

D. Yield ratios of light nuclei and antinuclei

Yield ratios of light (anti-)nuclei are more sensitive probes for the production mechanism and exhibit some interesting behaviors as functions of the collision energy and the collision centrality. In this subsection, we systematically study different kinds of yield ratios.

Figure 7 shows the ratios of antiparticles to particles \bar{p}/p , \bar{d}/d , and \bar{i}/t in the most central 0–10% centrality in Au-Au collisions at $\sqrt{s_{NN}} = 7.7, 11.5, 19.6, 27, 39, 54.4$ GeV. Filled squares are the data of \bar{p}/p from the STAR Collaboration [45], and filled circles with error bars are the data of \bar{d}/d [45]. Open pentagons and triangles connected with lines to guide the eye are the theoretical results for \bar{p}/p and \bar{d}/d , which agree well with the data. Open diamonds connected with lines to guide the eye are the theoretical predictions for \bar{i}/t . All these antiparticle-to-particle ratios increase and exhibit a distinct hierarchy with different constituent (anti-)nucleon numbers as the function of the collision energy. This is due to the decrease of net baryon density with the increasing energy. At very high collision energies, such as at

those at the LHC, it can be considered that the net baryon density is close to zero and all these ratios approach to one and their hierarchy with different constituent (anti-)nucleons disappear.

Figure 8 shows the energy dependence of two-particle ratios d/p , t/p , t/d and the corresponding antiparticle ratios \bar{d}/\bar{p} , \bar{i}/\bar{p} , \bar{i}/\bar{d} in the most central 0–10% centrality in Au-Au collisions at $\sqrt{s_{NN}} = 7.7, 11.5, 19.6, 27, 39, 54.4$ GeV. Filled symbols are the data in Refs. [43,45,56]. Open symbols connected with different lines to guide the eye are our results. The two-particle ratios d/p , t/p , t/d decrease while two-antiparticle ratios \bar{d}/\bar{p} , \bar{i}/\bar{p} , \bar{d}/\bar{p} increase as a function of $\sqrt{s_{NN}}$. With the increasing $\sqrt{s_{NN}}$, the net nucleons stopped in the midrapidity region decrease while the energy deposited to create antinucleons increases. This will enhance the antinucleon rapidity density and suppress the nucleon rapidity density. These two-particle ratios are related with the nucleon density, and two-antiparticle ratios are related with the antinucleon density. So they have different behaviors as a function of $\sqrt{s_{NN}}$. Values of d/p (\bar{d}/\bar{p}) are comparable to t/d (\bar{d}/\bar{p}), and

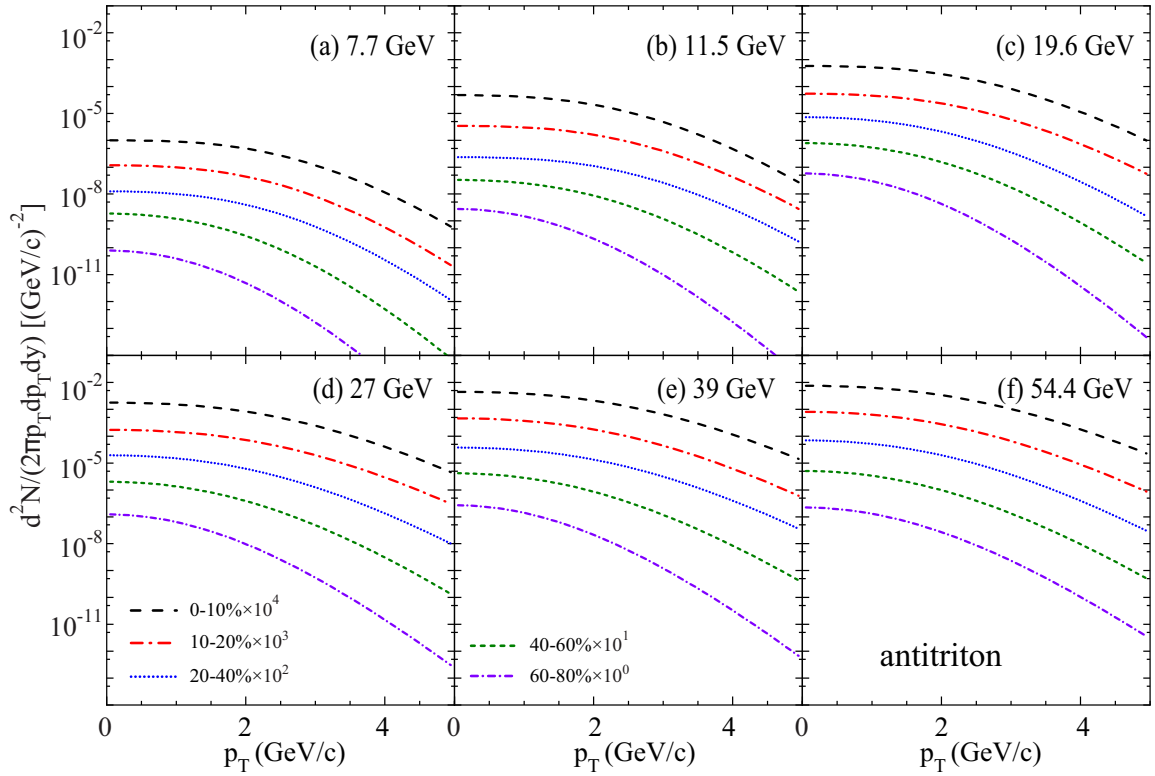


FIG. 6. Predictions for invariant p_T spectra of antitritons at midrapidity in Au-Au collisions in different centralities at $\sqrt{s_{NN}} = 7.7, 11.5, 19.6, 27, 39, 54.4$ GeV. Spectra for different centralities denoted by different lines are scaled by different factors for clarity.

they are much larger than those of t/p (\bar{t}/\bar{p}). This is due to d/p and t/d being proportional to the nucleon density while t/p is proportional to the square of the nucleon density. The similar case holds for two-antiparticle ratios.

Figures 9(a) and 9(b) show the energy dependence of ratios d/p^2 and \bar{d}/\bar{p}^2 , respectively, in Au-Au collisions in 0–10%, 10–20%, 20–40%, 40–60%, 60–80% centralities. Both d/p^2 and \bar{d}/\bar{p}^2 decrease with the increase of $\sqrt{s_{NN}}$, which is very

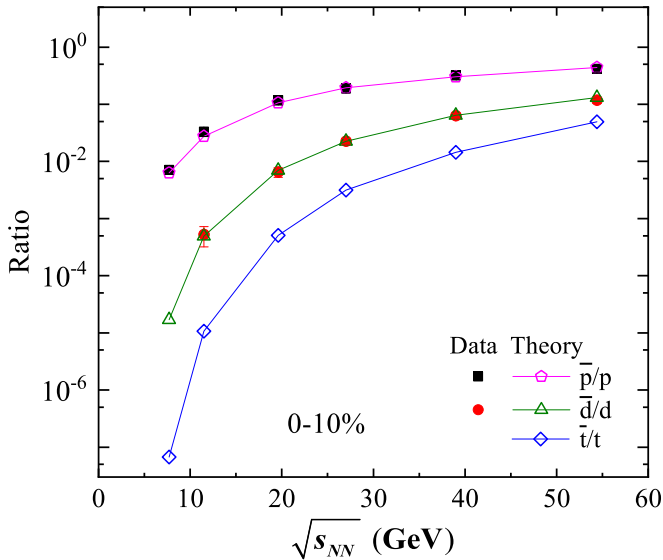


FIG. 7. Energy dependence of \bar{p}/p , \bar{d}/d and \bar{t}/t in the most central 0–10% Au-Au collisions. Data of \bar{p}/p and \bar{d}/d denoted by filled symbols are from Ref. [45]. Open triangles and diamonds connected with lines to guide the eye are the theoretical results for \bar{d}/d and \bar{t}/t , respectively.

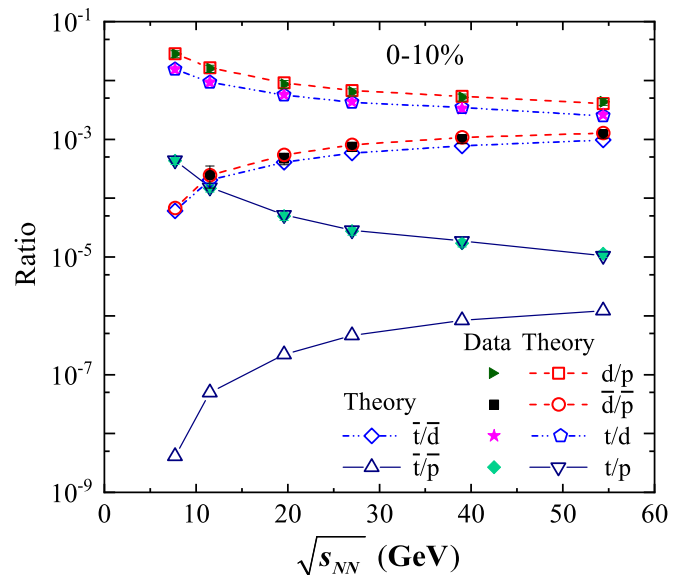


FIG. 8. Energy dependence of ratios d/p , t/p , t/d , \bar{d}/\bar{p} , \bar{t}/\bar{p} , and \bar{t}/\bar{d} in the most central 0–10% Au-Au collisions. Filled symbols are the data [43,45,56]. Open symbols connected with different lines to guide the eye are the theoretical results.

TABLE II. Yield densities dN/dy of d , \bar{d} , t , and \bar{t} at midrapidity in Au-Au collisions in different centralities at $\sqrt{s_{\text{NN}}} = 7.7, 11.5, 19.6, 27, 39, 54.4$ GeV. Data are from Refs. [43,45].

$\sqrt{s_{\text{NN}}}$	Centrality	d		\bar{d}		t		\bar{t}
		data	theory	data	theory	data	theory	theory
7.7 GeV	0–10 %	$140.99 \pm 0.41 \pm 10.97$	142.52	–	2.43	21.64	22.06	1.48
	10–20 %	$93.87 \pm 0.32 \pm 7.92$	96.73	–	1.94	15.76	16.51	1.41
	20–40 %	$49.06 \pm 0.16 \pm 5.38$	51.86	–	1.46	7.30	9.23	1.33
	40–60 %	$15.48 \pm 0.09 \pm 2.92$	16.52	–	0.89	1.25	1.44	1.25
	60–80 %	$3.13 \pm 0.05 \pm 0.91$	3.28	–	0.22	–	–	0.36
11.5 GeV	0–10 %	$63.05 \pm 0.14 \pm 4.55$	65.11	$3.29 \pm 0.63 \pm 1.10$	3.21	5.83	6.07	6.50
	10–20 %	$41.02 \pm 0.11 \pm 3.39$	42.46	$1.92 \pm 0.32 \pm 0.57$	2.31	4.00	4.23	4.94
	20–40 %	$21.92 \pm 0.06 \pm 2.23$	22.32	$1.05 \pm 0.17 \pm 0.34$	1.42	1.96	2.34	3.28
	40–60 %	$6.73 \pm 0.03 \pm 1.17$	6.96	–	0.84	0.34	0.34	3.01
	60–80 %	$1.31 \pm 0.02 \pm 0.40$	1.38	–	0.29	–	–	1.48
19.6 GeV	0–10 %	$27.45 \pm 0.06 \pm 2.04$	29.12	$17.88 \pm 0.52 \pm 3.14$	20.45	15.70	16.43	8.33
	10–20 %	$18.78 \pm 0.05 \pm 1.57$	20.09	$13.16 \pm 0.45 \pm 2.36$	15.38	10.20	11.98	6.92
	20–40 %	$9.73 \pm 0.03 \pm 1.00$	10.05	$10.33 \pm 0.27 \pm 1.87$	11.44	5.37	6.23	6.73
	40–60 %	$3.20 \pm 0.01 \pm 0.55$	3.30	$5.48 \pm 0.20 \pm 1.15$	6.65	0.90	0.95	6.10
	60–80 %	$0.68 \pm 0.007 \pm 0.21$	0.67	$2.07 \pm 0.14 \pm 0.70$	2.23	–	–	2.80
27 GeV	0–10 %	$18.44 \pm 0.04 \pm 1.28$	19.57	$41.35 \pm 0.54 \pm 4.63$	44.34	7.98	8.35	2.59
	10–20 %	$12.83 \pm 0.03 \pm 1.05$	12.98	$32.35 \pm 0.47 \pm 3.85$	35.17	5.07	5.71	2.35
	20–40 %	$6.84 \pm 0.01 \pm 0.70$	7.05	$23.03 \pm 0.28 \pm 2.79$	24.68	3.17	3.38	2.09
	40–60 %	$2.33 \pm 0.009 \pm 0.43$	2.45	$11.48 \pm 0.21 \pm 2.45$	12.92	0.49	0.59	1.55
	60–80 %	$0.49 \pm 0.004 \pm 0.17$	0.52	$3.33 \pm 0.11 \pm 1.23$	3.87	–	–	0.60
39 GeV	0–10 %	$12.73 \pm 0.02 \pm 0.95$	13.27	$79.96 \pm 0.46 \pm 6.35$	85.57	4.21	4.59	6.60
	10–20 %	$8.78 \pm 0.01 \pm 0.69$	9.20	$62.39 \pm 0.40 \pm 4.60$	64.75	3.01	3.32	5.80
	20–40 %	$4.81 \pm 0.008 \pm 0.48$	5.03	$41.24 \pm 0.23 \pm 4.11$	42.81	1.68	1.92	4.46
	40–60 %	$1.72 \pm 0.004 \pm 0.30$	1.82	$19.24 \pm 0.15 \pm 3.26$	22.45	0.36	0.37	3.33
	60–80 %	$0.37 \pm 0.002 \pm 0.12$	0.37	$5.50 \pm 0.09 \pm 1.80$	6.77	–	–	1.33
54.4 GeV	0–10 %	10.28	9.58	1.21	1.26	2.67	2.47	1.22
	10–20 %	7.07	7.15	0.93	0.93	2.36	2.14	0.94
	20–40 %	3.89	3.67	0.57	0.59	1.29	1.16	0.69
	40–60 %	1.40	1.27	0.28	0.28	0.25	0.21	0.39
	60–80 %	0.31	0.28	0.07	0.08	–	–	0.13

different from the previous d/p and \bar{d}/\bar{p} . Note that d/p^2 and \bar{d}/\bar{p}^2 represent the probability of any nucleon-pair coalescing into a deuteron and that of any antinucleon-pair coalescing into an antideuteron. They do not depend on the absolute (anti-)nucleon numbers or the (anti-)nucleon rapidity densities, but are sensitive to the fundamental production mechanism. It is more difficult for any (anti-)nucleon pair to recombine into (anti-)deuteron in a larger hadronic system. So d/p^2 and \bar{d}/\bar{p}^2 decrease with increasing $\sqrt{s_{\text{NN}}}$.

We want to point out that (anti-)protons in the ratios mentioned above are referred to those final-state ones including those from hyperon weak decays. As is well known, (anti-)nucleons taking part in forming light (anti-)nuclei are those created before the kinetic freeze-out, not including those from hyperon weak decays. To probe the production properties more directly, one should use (anti-)nucleons excluding hyperon weak decay contaminations, i.e., those at

the kinetic freeze-out, to construct ratios. Here, we present d/p_{kin}^2 and $\bar{d}/\bar{p}_{\text{kin}}^2$ in Fig. 9(c) and 9(d) where the subscript *kin* denotes (anti-)protons at the kinetic freeze-out. It can be found that d/p_{kin}^2 and $\bar{d}/\bar{p}_{\text{kin}}^2$ almost coincide with each other after correcting the weak decays of (anti-)protons from (anti-)hyperons. This further indicates that the intrinsic dynamics of two nucleons recombining into a deuteron is similar with that of two antinucleons recombining into an antideuteron.

E. Multiparticle yield correlation tp/d^2

In this subsection, we study the multiparticle yield correlation tp/d^2 , which has recently attracted extensive attention [32,46,59–62] and considered to be a probe for the structure of the QCD phase diagram [6,34,62]. Compared with other yield ratios discussed in the last subsection, it has been observed by the STAR experiment to show a nonmonotonic trend as

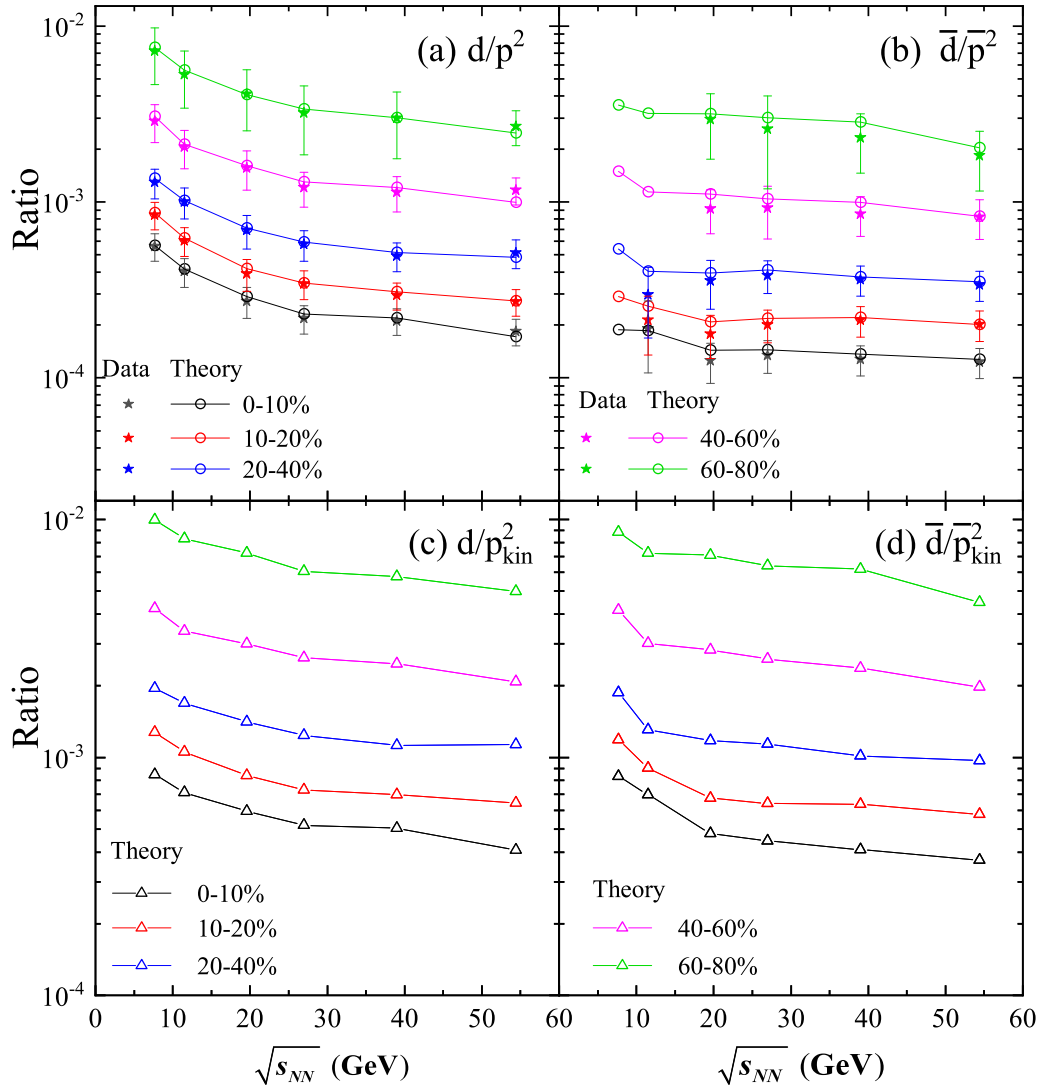


FIG. 9. Energy dependence of (a) d/p^2 , (b) \bar{d}/\bar{p}^2 , (c) d/p_{kin}^2 , and (d) $\bar{d}/\bar{p}_{\text{kin}}^2$ at midrapidity in Au-Au collisions in different centralities. Data denoted by filled symbols with error bars are obtained according to the final-state proton and deuteron yields from STAR Collaboration [43,45,56]. Open circles and triangles connected with lines to guide the eye are the theoretical results with final-state protons and kinetic freeze-out ones, respectively.

the function of $\sqrt{s_{NN}}$ in the most central Au-Au collisions as shown by the solid circles and squares with error bars in Fig. 10(a). Note that solid circles are obtained based on the yields of tritons, deuterons, and final-state protons measured in Refs. [43,45,56], and solid squares are the STAR preliminary data in which the proton yield has been corrected by weak-decay feed down from strange baryons based on the UrQMD simulation [63]. The peak around 20 GeV in these solid symbols is considered in some works to be a signal of an enhanced baryon density fluctuation and therefore a possible signal of potentially a critical point [34,46].

To further ascertain the reliability of tp/d^2 as a probe of a large baryon density fluctuation near the critical point and/or production mechanism of light nuclei, different methods of correcting the weak decay contamination for protons are necessary. We here first use a data-driven weak decay correction for the proton to get the data of tp/d^2 , i.e.,

$p \approx p_{\text{withWD}} - 63.9\%(\Lambda + 2\Xi^-)$, in which p_{withWD} refers to those including weak decay contaminations measured at the current experiment and Λ , Ξ^- denote the measured primary Λ , Ξ^- at experiments. The factor 2 before Ξ^- is to include Ξ^0 weak decay contaminations to protons. Note that the weak decay correction for the proton from Σ^+ is not included due to the deficiency of Σ^+ data in present experiments in this data-driven weak decay correction method. The filled stars with error bars in Fig. 10(a) are the experimental data after correcting Λ and Ξ weak decay contaminations [64] for protons, which are much smaller than those solid circles and also much smaller than those solid squares. Peak behavior around 20 GeV is weakened in the Λ and Ξ data-driven weak decay correction result for tp/d^2 compared to that without weak decay corrections. Open triangles connected with lines to guide the eye are our results without weak decay corrections, which basically agree with the data and exhibit

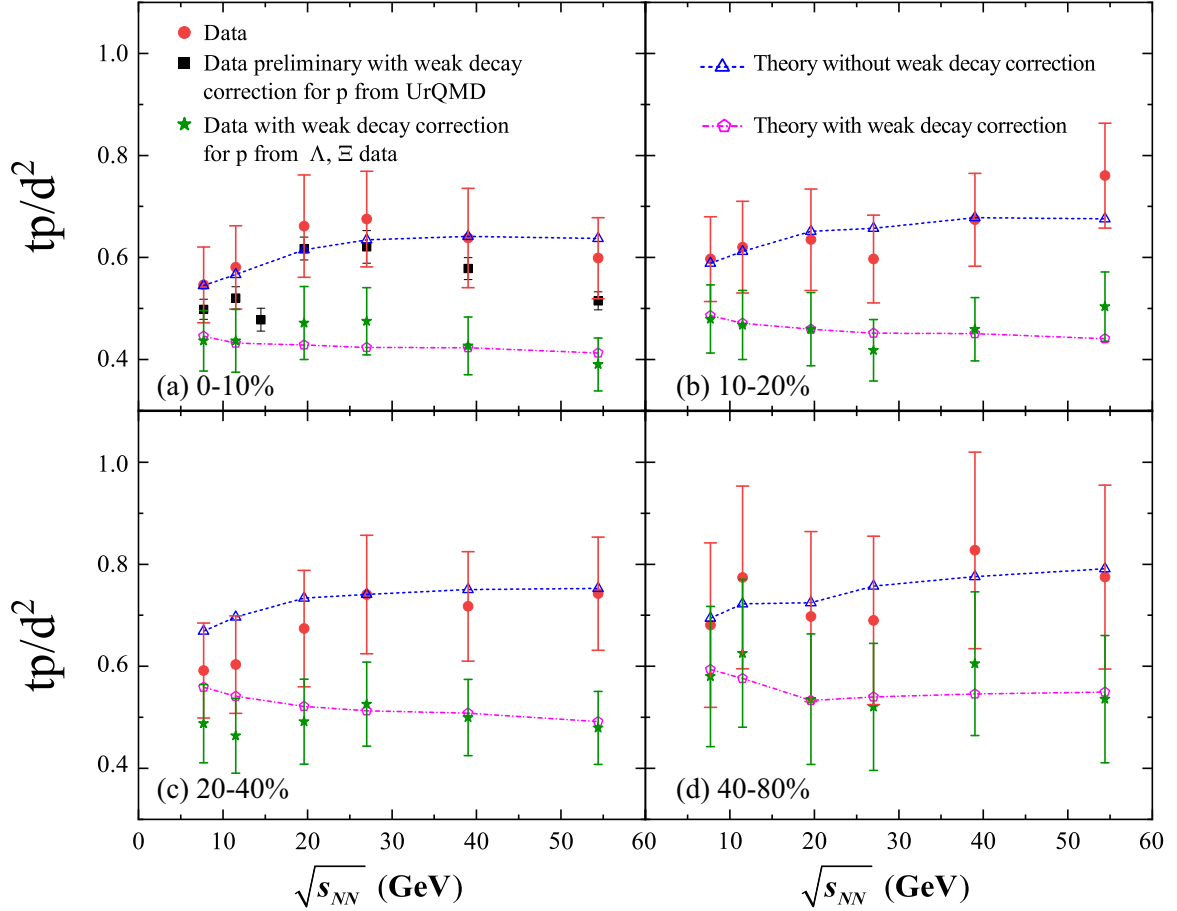


FIG. 10. Energy dependence of tp/d^2 in different centralities at midrapidity in Au-Au collisions. Data denoted by filled circles are obtained based on the yields of tritons, deuterons, and final-state protons in Refs. [43,45,56], and data preliminary with weak decay correction for p from UrQMD denoted by filled squares are from Ref. [43]. Theoretical results without weak decay corrections for protons are open triangles and those with weak decay corrections are open pentagons.

an increasing trend and then seems invariant at $\sqrt{s_{NN}} > 27$ GeV. Open pentagons connected with lines to guide the eye are our corresponding theoretical results with weak decay corrections, where we use SDQCM to correct the decay contaminations from strange hyperons, including Λ^0 , Σ^+ , $\Xi^{0,-}$, and Ω^- . Their weak decays into protons take about 61–64 %, 13–14 %, 20–24 %, and 1–2 %, respectively, of all weak decay protons, when the strangeness factor is in the range 0.4–0.5 in heavy ion collisions [65]. Our theoretical results with weak decay corrections denoted by open pentagons exhibit a very slightly decreasing trend and agree with the data within error bars. Comparing the result without weak decay correction with that with weak decay correction, one can see that protons from hyperon weak decays have different influences on the behavior of tp/d^2 at different collision energies, i.e., the weak decay contamination for tp/d^2 is different at different collision energies.

We also study tp/d^2 in other centralities and results are given in Fig. 10(b)–10(d). In these three centralities, there seems to be no peak behaviors in the function of $\sqrt{s_{NN}}$. Theoretical results without weak decay corrections denoted by open triangles increase slightly and then become invariant, and those with weak decay corrections denoted by open

pentagons decrease slightly. All theoretical results agree with the data within error bars. The different behaviors for open triangles and pentagons come from different contributions of protons from hyperon weak decays. With the increasing energy, the decay contribution becomes stronger. This makes the decreasing trend of without-weak-decay-correction results to be increasing, or invariant behavior of with-weak-decay-correction results. This further shows that tp/d^2 should be carefully corrected from hyperon weak decays for protons to probe the production characteristics of light nuclei and the structure of the QCD phase diagram.

IV. SUMMARY

Based on the description of the production of different mesons and baryons by the SDQCM, we obtained p_T distributions of final-state (anti-)protons as well as those produced at the kinetic freeze-out in Au-Au collisions at $\sqrt{s_{NN}} = 7.7, 11.5, 19.6, 27, 39, 54.4$ GeV. We found that weak decay contaminations for protons from Λ and Σ hyperons were different in different centralities at different collision energies. With these momentum distributions of kinetic freeze-out protons and antiprotons obtained from the SDQCM, we studied

the production of light nuclei and antinuclei in the (anti-)nucleon coalescence mechanism in relativistic heavy ion collisions at energies employed at the RHIC beam energy scan.

We first computed the p_T spectra of (anti-)deuterons (d , \bar{d}) and (anti-)tritons (t , \bar{t}) in Au-Au collisions at $\sqrt{s_{NN}} = 7.7, 11.5, 19.6, 27, 39, 54.4$ GeV and found the available experimental data for these p_T spectra can be well reproduced. On this basis, we gave the predictions of p_T spectra for \bar{d} at 11.5 GeV for 60–80% and 7.7 GeV and \bar{t} at these energies. We then studied the yield densities of light (anti-)nuclei and our results were consistent with the available data.

We finally studied different yield ratios, such as \bar{d}/d , \bar{t}/t , d/p , \bar{d}/\bar{p} , t/p , \bar{t}/\bar{p} , t/d , \bar{t}/\bar{d} , d/p^2 , \bar{d}/\bar{p}^2 , etc., and naturally explained their interesting behaviors as the function of the collision energy. We especially studied the multiparticle yield correlation tp/d^2 and pointed out that it should be carefully corrected from hyperon weak decays for protons

to employ it to probe the production characteristics of light nuclei and the structure of the QCD phase diagram. All of our results showed that the coalescence mechanism for nucleons and antinucleons played a dominant role for the production of light nuclei and antinuclei at RHIC beam energy scan energies.

ACKNOWLEDGMENTS

We thank Xiao-Feng Luo for helpful discussions. This work was supported in part by the National Natural Science Foundation of China under Grants No. 12175115 and No. 11975011, the Natural Science Foundation of Shandong Province, China, under Grants No. ZR2020MA097, No. ZR2019YQ06, and No. ZR2019MA053, and Higher Educational Youth Innovation Science and Technology Program of Shandong Province under Grants No. 2020KJJ004 and No. 2019KJJ010.

-
- [1] J. L. Nagle, B. S. Kumar, M. J. Bennett, G. E. Diebold, J. K. Pope, H. Sorge, and J. P. Sullivan, *Phys. Rev. Lett.* **73**, 1219 (1994).
- [2] J. Chen, D. Keane, Yu-Gang Ma, A. Tang, and Zhangbu Xu, *Phys. Rep.* **760**, 1 (2018).
- [3] K. Blum and M. Takimoto, *Phys. Rev. C* **99**, 044913 (2019).
- [4] J. Aichelin, *Phys. Rep.* **202**, 233 (1991).
- [5] P. von Doetinchem, K. Perez, T. Aramaki, S. Baker, and S. Barwick, *J. Cosmol. Astropart. Phys.* **08** (2020) 035.
- [6] K. J. Sun, L. W. Chen, C. M. Ko, J. Pu, and Z. B. Xu, *Phys. Lett. B* **781**, 499 (2018).
- [7] Z. Citron *et al.*, CERN Yellow Rep. Monogr. **7**, 1159 (2019).
- [8] P. Braun-Munzinger and B. Dönigus, *Nucl. Phys. A* **987**, 144 (2019).
- [9] D. Oliinychenko, *Nucl. Phys. A* **1005**, 121754 (2021).
- [10] A. Bzdak, Shin'ichi Esumi, V. Koch, J. Liao, M. Stephanov, and Nu Xu, *Phys. Rep.* **853**, 1 (2020).
- [11] A. Mekjian, *Phys. Rev. Lett.* **38**, 640 (1977).
- [12] P. J. Siemens and J. I. Kapusta, *Phys. Rev. Lett.* **43**, 1486 (1979).
- [13] A. Andronic, P. Braun-Munzinger, J. Stachel, and H. Stöcker, *Phys. Lett. B* **697**, 203 (2011).
- [14] J. Cleymans, S. Kabana, I. Kraus, H. Oeschler, K. Redlich, and N. Sharma, *Phys. Rev. C* **84**, 054916 (2011).
- [15] A. Andronic, P. Braun-Munzinger, K. Redlich, and J. Stachel, *Nature (London)* **561**, 321 (2018).
- [16] Y. Cai, T. D. Cohen, B. A. Gelman, and Y. Yamauchi, *Phys. Rev. C* **100**, 024911 (2019).
- [17] W. Zhao, L. Zhu, H. Zheng, Che Ming Ko, and H. Song, *Phys. Rev. C* **98**, 054905 (2018).
- [18] J. I. Kapusta, *Phys. Rev. C* **21**, 1301 (1980).
- [19] S. T. Butler and C. A. Pearson, *Phys. Rev.* **129**, 836 (1963).
- [20] A. Schwarzschild and C. Zupancic, *Phys. Rev.* **129**, 854 (1963).
- [21] H. Sato and K. Yazaki, *Phys. Lett. B* **98**, 153 (1981).
- [22] C. B. Dover, U. Heinz, E. Schnedermann, and J. Zimányi, *Phys. Rev. C* **44**, 1636 (1991).
- [23] R. Mattiello, A. Jahns, H. Sorge, H. Stöcker, and W. Greiner, *Phys. Rev. Lett.* **74**, 2180 (1995).
- [24] J. L. Nagle, B. S. Kumar, D. Kusnezov, H. Sorge, and R. Mattiello, *Phys. Rev. C* **53**, 367 (1996).
- [25] R. Mattiello, H. Sorge, H. Stöcker, and W. Greiner, *Phys. Rev. C* **55**, 1443 (1997).
- [26] L.-W. Chen, C. M. Ko, and B.-A. Li, *Phys. Rev. C* **68**, 017601 (2003).
- [27] A. Polleri, J. P. Bondorf, and I. N. Mishustin, *Phys. Lett. B* **419**, 19 (1998).
- [28] R. Scheibl and U. Heinz, *Phys. Rev. C* **59**, 1585 (1999).
- [29] N. Sharma, T. Perez, A. Castro, L. Kumar, and C. Nattrass, *Phys. Rev. C* **98**, 014914 (2018).
- [30] S. Bazak and S. Mrówczyński, *Mod. Phys. Lett. A* **33**, 1850142 (2018).
- [31] H. H. Gutbrod *et al.*, *Phys. Rev. Lett.* **37**, 667 (1976).
- [32] W. Zhao, C. Shen, C. M. Ko, Q. Liu, and H. Song, *Phys. Rev. C* **102**, 044912 (2020).
- [33] S. Acharya *et al.* (ALICE Collaboration), *Phys. Lett. B* **811**, 135849 (2020).
- [34] H. Liu, D. Zhang, S. He, K. J. Sun, N. Yu, and X. Luo, *Phys. Lett. B* **805**, 135452 (2020).
- [35] F. X. Liu, G. Chen, Z. L. Zhe, D. m. Zhou, and Y. L. Xie, *Eur. Phys. J. A* **55**, 160 (2019).
- [36] Y. Oh, Z. W. Lin, and C. M. Ko, *Phys. Rev. C* **80**, 064902 (2009).
- [37] D. Oliinychenko, L. G. Pang, H. Elfner, and V. Koch, *Phys. Rev. C* **99**, 044907 (2019).
- [38] D. Oliinychenko, C. Shen, and V. Koch, *Phys. Rev. C* **103**, 034913 (2021).
- [39] J. Staudenmaier, D. Oliinychenko, J. M. Torres-Rincon, and H. Elfner, *Phys. Rev. C* **104**, 034908 (2021).
- [40] S. Afanasiev *et al.* (PHENIX Collaboration), *Phys. Rev. Lett.* **99**, 052301 (2007).
- [41] L. Adamczyk *et al.* (STAR Collaboration), *Phys. Rev. C* **94**, 034908 (2016).
- [42] L. Adam *et al.* (STAR Collaboration), *Phys. Rev. C* **102**, 044906 (2020).
- [43] D. Zhang (STAR Collaboration), *Nucl. Phys. A* **1005**, 121825 (2021).

- [44] C. Adler *et al.* (STAR Collaboration), *Phys. Rev. Lett.* **87**, 262301 (2001).
- [45] J. Adam *et al.* (STAR Collaboration), *Phys. Rev. C* **99**, 064905 (2019).
- [46] Kai-Jia Sun, Che Ming Ko, Feng Li, Jun Xu, and Lie-Wen Chen, *Eur. Phys. J. A* **57**, 313 (2021).
- [47] J. Song, X. F. Wang, H. H. Li, R. Q. Wang, and F. L. Shao, *Phys. Rev. C* **103**, 034907 (2021).
- [48] Y. T. Feng, J. Song, and F. L. Shao, Centrality and energy dependence of strange hadron production in Au+Au collisions at $\sqrt{s_{NN}}=7.7$ to 54.4 GeV at RHIC (unpublished).
- [49] R. Q. Wang, F. L. Shao, and J. Song, *Phys. Rev. C* **103**, 064908 (2021).
- [50] R. Q. Wang, J. Song, G. Li, and F. L. Shao, *Chin. Phys. C* **43**, 024101 (2019).
- [51] L. W. Chen, C. M. Ko, and B. A. Li, *Nucl. Phys. A* **729**, 809 (2003).
- [52] Lilin Zhu, Che Ming Ko, and Xuejiao Yin, *Phys. Rev. C* **92**, 064911 (2015).
- [53] S. Mrówczyński, *Acta Phys. Pol. B* **48**, 707 (2017).
- [54] I. Angeli and K. P. Marinova, *At. Data Nucl. Data Tables* **99**, 69 (2013).
- [55] J. Song, F. L. Shao, and Z. T. Liang, *Phys. Rev. C* **102**, 014911 (2020).
- [56] L. Adamczyk *et al.* (STAR Collaboration), *Phys. Rev. C* **96**, 044904 (2017).
- [57] M. A. Lisa, S. Pratt, R. Soltz, and U. Wiedemann, *Annu. Rev. Nucl. Part. Sci.* **55**, 357 (2005).
- [58] J. Adam *et al.* (ALICE Collaboration), *Phys. Rev. C* **93**, 024905 (2016).
- [59] K. J. Sun, C. M. Ko, and Z. W. Lin, *Phys. Rev. C* **103**, 064909 (2021).
- [60] K. J. Sun, F. Li, and C. M. Ko, *Phys. Lett. B* **816**, 136258 (2021).
- [61] W. Zhao, K. J. Sun, C. M. Ko, and X. Luo, *Phys. Lett. B* **820**, 136571 (2021).
- [62] K. J. Sun, L. W. Chen, C. M. Ko, and Z. Xu, *Phys. Lett. B* **774**, 103 (2017).
- [63] L. Adamczyk *et al.* (STAR Collaboration), *Phys. Rev. Lett.* **121**, 032301 (2018).
- [64] J. Adam *et al.* (STAR Collaboration), *Phys. Rev. C* **102**, 034909 (2020).
- [65] R. Q. Wang, F. L. Shao, J. Song, Q. B. Xie, and Z. T. Liang, *Phys. Rev. C* **86**, 054906 (2012).